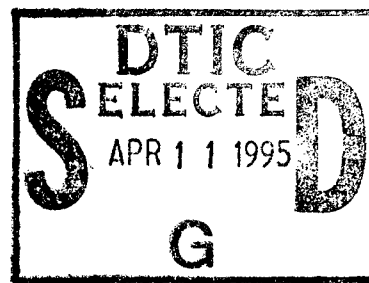PL-TR-94-2190

A PROTOTYPE IONOSPHERIC TOMOGRAPHY SYSTEM (ITS)

E. J. Fremouw
J. A. Secan

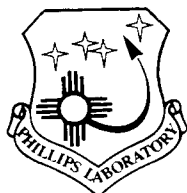Northwest Research Associates, Inc.
300 120th Avenue, NE
Building 7, Ste 220
Bellevue, WA 98005

DTIC
SELECTED
APR 1 1 1995
G

15 June 1994

Final Report
30 July 1991 - 30 April 1994

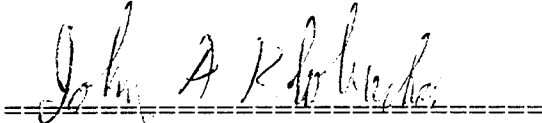## PHILLIPS LABORATORY
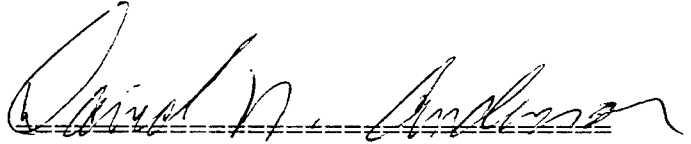## Directorate of Geophysics
AIR FORCE MATERIEL COMMAND
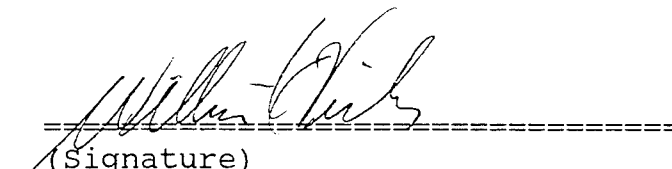## HANSCOM AFB, MA 01731-3010

19950407 155

"This technical report has been reviewed and is approved for publication"

_____
(Signature)
John A. Klobuchar
Contract Manager

_____
(Signature)
David N. Anderson
Branch Chief

_____
(Signature)
William K. Vickery
Division Director

This report has been reviewed by the ESC Public Affairs Office (PA) and is releasable to the National Technical Information Service (NTIS)

Qualified requestors may obtain additional copies from the Defense Technical Information Center (DTIC). All others should apply to the National Technical Information Service (NTIS).

If your address has changed, if you wish to be removed from the mailing list, or if the addressee is no longer employed by your organization, please notify "PL/TSI, 29 Randolph Road, Hanscom AFB, MA 01731-3010. This will assist us in maintaining a current mailing list.

Do not return copies of this report unless contractual obligations or notices on a specific document requires that it be returned.

REPORT DOCUMENTATION PAGE

Form Approved
OMB No. 0704-0188

1. AGENCY USE ONLY *(Leave blank)*	2. REPORT DATE 15 June 1994	3. REPORT TYPE AND DATES COVERED Final Report, 30 July 1991 - 30 April 1994

4. TITLE AND SUBTITLE
A Prototype Ionospheric Tomography System (ITS)

5. FUNDING NUMBERS

F19628-90-C-0116
PE 65502F
PR 5502
TA 07
WU AD

6. AUTHOR(S)
E. J. Fremouw and J. A. Secan

7. PERFORMING ORGANIZATION NAME(S) AND ADDRESS(ES)
Northwest Research Associates, Inc.
300 120th Ave NE, Bldg 7, Ste 220
P.O. Box 3027
Bellevue, WA 98009-3027

8. PERFORMING ORGANIZATION REPORT NUMBER
NWRA-CR-94-R117

9. SPONSORING / MONITORING AGENCY NAME(S) AND ADDRESS(ES)
Phillips Laboratory
29 Randolph road
Hanscom AFB, MA 01731-3010
Contract Manager: J.A. Klobuchar/GPIM

10. SPONSORING / MONITORING AGENCY REPORT NUMBER
PL-TR-94-2190

11. SUPPLEMENTARY NOTES The authors have removed all proprietary information from this SBIR report.

12a. DISTRIBUTION / AVAILABILITY STATEMENT

approved for public release; distribution unlimited

12b. DISTRIBUTION CODE

13. ABSTRACT *(Maximun 200 words)*

Northwest Research Associates has developed a prototype ionospheric tomography system (ITS) for use with the "Transit" satellites of the U.S. Navy Navigation Satellite System (NNSS). The NNSS satellites transmit coherent signals at 150 and 400 MHz. The ITS consists of a data-collection subsystem made up of five newly designed, largely digital ITS10S coherent radio receivers for recording dispersive phase between the two NNSS signals, a data-retrieval subsystem, and a central processor. In addition to dispersive phase, the receivers measure the signal intensities, all at 50 samples per sec (sps), for recording signal scintillation due to scattering in medium-scale (of order km) plasma-density irregularities. The dispersive phase is smoothed to one sps for use as a measure of the path-integral of plasma density (the "total electron content," or TEC). Data may be retrieved from on-line personal computers associated with each receiver either on diskettes or by means of modems that constitute the primary data-retrieval subsystem. The data-retrieval subsystem also includes one "data collection platform" for satellite relay of data from a remote station to CONUS for subsequent modem retrieval. The central processor consists of six FORTRAN programs developed for tomographic inversion of TEC data by means of a weighted, damped, least-squares formulation of discrete inverse theory. This report describes application of that theory to the central processor and briefly describes the data-collection and data-retrieval subsystems.

14. SUBJECT TERMS
Ionospheric tomography, Plasma density, Radio refractive index, Radiowave scintillation, Total electron content

15. NUMBER OF PAGES
30

16. PRICE CODE

17. SECURITY CLASSIFICATION OF REPORT Unclassified	18. SECURITY CLASSIFICATION OF THIS PAGE Unclassified	19. SECURITY CLASSIFICATION OF ABSTRACT Unclassified	20. LIMITATION OF ABSTRACT SAR

Table of Contents

List of Figures

A PROTOTYPE IONOSPHERIC TOMOGRAPHY SYSTEM (ITS)

1. INTRODUCTION

Under this Small Business Innovative Research (SBIR) contract from Phillips Lab (PL) of Air Force Materiel Command, Northwest Research Associates (NWRA) has developed a prototype ionospheric tomography system (ITS). Capable of producing two-dimensional images of the ionosphere, the ITS comprises three subsystems: data collection, data retrieval, and central processing. The data-collection subsystem consists of five NWRA ITS10S receivers, together with their antennas and five on-line personal computers (PCs). The data-retrieval subsystem consists primarily of five 14.4-kbaud modems, one associated with each receiver/PC. In addition, it includes a single Data Collection Platform (DCP) for use as part of the Geostationary Operational Environmental Satellite (GOES) Data Collection System. In the event of location at a remote field site, the GOES DCP may be deployed with any of the five receivers for retransmission of raw data via GOES. Whether retrieved via direct modem connection or relayed through GOES, the recorded data are analyzed by means of the central processor, which is made up of six FORTRAN programs that run on the user's work station.

The raw data collected by means of the receivers consist primarily of dispersive phase (to within an unknown constant) between the VHF and UHF (150 and 400-MHz) signals transmitted from the low-orbiting "Transit" satellites of the U.S. Navy Navigation Satellite System (NNSS). At the central processor, the dispersive-phase measurements are converted to relative "total electron content" (TEC), which is the integral of plasma density along the time-sequential lines of sight between the source Transit and each receiver. Based on the observing geometry, which it computes from NNSS orbital information, the central processor tomographically inverts the relative TEC measurements to infer a two-dimensional (altitude vs. latitude) map of plasma density, which it stores for plotting by the user as an "image" of the ionosphere.

In addition to dispersive phase, each ITS10S records the intensities of the VHF and UHF signals received from the Transit, each of the three measurements being made at 50 samples per sec (sps). Thus, the raw data may be used for assessment and analysis of radiowave scintillation produced by refracting and diffracting plasma-density structures in the ionosphere. For diagnostic purposes, the dispersive-phase and intensity scintillation indices are computed by the data-collection subsystem's PCs for each 20-sec interval in a satellite pass. The indices are transmitted via the data-retrieval subsystem, together with one-sec values of smoothed dispersive phase to be converted to TEC. The raw data (in the form of UHF intensity and the VHF in-phase and phase-quadrature components relative to UHF phase) are stored on the hard disk of each station PC and may be written to diskettes for more detailed scintillation analysis if desired.

In Section 2 of this report, we describe the central processor, starting with its underlying theory of tomographic inversion. Sections 3 and 4 contain brief descriptions of the data-recording and data-retrieval subsystems. We conclude with recommendations in Section 5.

2. TOMOGRAPHIC INVERSION IN THE CENTRAL PROCESSOR

2.1. Background

Among the techniques available for tomographically inverting path-integral measurements of plasma density (i.e., TEC data) to image the ionosphere, those employing discrete inverse theory (DIT) hold substantial promise. In our final report on Phase I of this SBIR contract (Fremouw et al 1990, hereinafter referred to as Ref. 1), we described such a linear algebraic approach and presented sample inversions employing a weighted, damped, least-squares (WDLS) procedure and simulated absolute TEC data. The WDLS procedure offers the advantage of an orderly means by which to introduce a-priori information about the **statistical** behavior of plasma-density structures in the ionosphere. In our implementation, deterministic a-priori information is limited to a latitudinally uniform background profile; departures therefrom that are reflected in the TEC data need not be weak.

Early in Phase II, we devised a pre-processor to resolve the ambiguity in received dispersive phase to convert relative TEC to absolute TEC (Fremouw and Lansinger, 1992a). Subsequently, however, we found that modest errors in resolving the ambiguous constant could destroy efficacy of the ensuing tomographic inversion of absolute TEC (Fremouw and Lansinger, 1992b). Estimating the unknown constant along with the plasma-density field as elements of the same WDLS solution has proven to be a far superior approach. Thus, our prototype central processor directly employs **relative** TEC data, without need for prior ambiguity resolution. In Section 2.1.1, we review the theoretical basis underlying our WDLS procedure, including its use with relative TEC. Simulated results from the processor are presented in Section 2.1.2.

2.1.1. Theory

The absolute-TEC forward problem may be discretized by representing the dispersive phase, ϕ_h, observed on a path, h, plus its $2n_h\pi$ ambiguity minus any unknown dispersion offset, $\Delta\phi_h$, arising in the receiver and/or transmitter as proportional (via a constant, C) to the sum of TEC increments accumulated in cells, i, as follows:

$$\phi_h + 2n_h\pi - \Delta\phi_h = C\sum_i N_{ei}\, ds_{hi} \quad, \tag{1}$$

where N_{ei} is the local mean electron density in the cell and ds_{hi} is the elemental length of the path in the cell.

The inverse problem is to estimate the N_{ei} from a multi-path set of ϕ_h. To begin, we postulate a representative background profile (height-dependent mean values of density in a gaussian ensemble of ionospheric profiles) and suppose it to be subtracted from the N_{ei} to obtain a perturbation field, δN_{ei}. We also compute the dispersive-phase contribution of the background and subtract it from the measured ϕ_h to obtain the following set of perturbation data, δ_h:

$$\delta_h = C\sum_i \delta N_{ei}\, ds_{hi} - 2n_h\pi + \Delta\phi_h \quad. \tag{2}$$

To address the **relative**-TEC problem, we note that the ambiguity is the same for all paths terminating at the same receiver so long as the receiver obtains a continuous record, and we assume that both receiver and transmitter offsets remain constant (although they may be of any magnitude) over the duration of the record. This being the case, subtracting the same datum, δ_0 (e.g., the first

2

one) from all values obtained by a given receiver (along with their identical ambiguities and offsets) results in

$$\delta_h - \delta_0 = C \sum_i \delta N_{ei} \, (ds_{hi} - ds_{0i}) \, , \tag{3}$$

where ds_{0i} is the pathlength of the reference ray through the ith cell (zero for most cells). That is [after dividing through by C to obtain $d_h = (\delta_h - \delta_0)/C$], we have the following relative-TEC forward problem:

$$d_h = \sum_i \delta N_{ei} (ds_{hi} - ds_{0i}) \, . \tag{4}$$

Our objective is to estimate δN_{ei}, to which we shall add the background profile to obtain estimates of N_{ei}.

The one-dimensional array of d_h values (the multi-receiver TEC data set with the reference value for each receiver subtracted from its subset) constitutes a "data vector," **d**. For reasons described in Ref. 1, we choose to represent the two-dimensional (altitude and geomagnetic latitude, say) field of δN_{ei} by means of two-dimensional basis functions and corresponding coefficients. Specifically, we expand it horizontally into a Fourier series of sines and cosines and vertically into a short series of empirical orthonormal functions (EOFs). This transforms the problem into estimating a "model vector", **m**, the elements, m_k, of which are coefficients to be applied to multiplied pairs of horizontal and vertical basis functions. [For specifics, see Section 2 B of Ref. 1.]

In matrix notation, the transformed forward problem is

$$\mathbf{d} = \mathbf{Gm} + \mathbf{n} \, , \tag{5}$$

where **G** is the geometry matrix describing the dependence of the data on the model parameters, with elements

$$G_{hk} = \partial d_h / \partial m_k \, , \tag{6}$$

and **n** is a "noise vector" whose elements, n_k, quantify the rms uncertainty due to dispersive-phase noise and model deficiency. The modeling procedure suffers from deficiencies such as the use of finite Fourier and EOF series, and these can be estimated. The uncertainty estimates can be different on different paths due to such variables as range-squared loss and the pathlengths through structures not accounted for in the finite basis-function series.

With the forward problem formulated as in Eq. (5), the inverse problem becomes that of employing a generalized inverse (Menke, 1989) matrix, $\mathbf{G^{-g}}$, to solve the equation for an estimated model vector, as follows:

$$\mathbf{\hat{m}} = \mathbf{G^{-g}} \, \mathbf{d} \, . \tag{7}$$

The central aspect of the procedure is to find $\mathbf{G^{-g}}$. Once that is accomplished and data are in hand, the matrix multiplication described by Eq. (7) is straightforward, as is transforming the resulting "model" (i.e., the estimated coefficients and their corresponding basis functions) into configuration space and adding the background profile removed in going from Eq. (1) to Eq. (2).

As described in Section 2 B of Ref. 1, we employ the following generalized inverse for the weighted, damped, least-squares problem:

3

$$G^{-g} = vG^T(GvG^T + e)^{-1} \,,\tag{8}$$

where ^{T} and $^{-1}$ stand for transpose and standard inverse, respectively, and where $\mathbf{v}$ and $\mathbf{e}$ are the a-priori covariance matrices of $\mathbf{m}$ and $\mathbf{n}$, respectively. In practice, we take the covariance matrices to be diagonal, so they become variance vectors (and, hence, we represent them by lower-case letters in our present notation).

While Eq. (5) et seq. are formally identical to their counterparts in Ref. 1, there is an important difference between $\mathbf{G}$ here and that in the previous work. If we denote the geometry matrix for the absolute-TEC problem dealt with in Ref. 1 by $\mathbf{G_{ab}}$, then its counterpart in the relative-TEC problem introduced here may be written as

$$\mathbf{G} = \mathbf{G_{ab}} - \mathbf{G_0} \,,\tag{9}$$

where $\mathbf{G_0}$ describes the dependence of the reference-ray measurements (one for each receiver) on the model parameters. This difference accounts for the subtraction on the right-hand side of Eqs. (3) and (4). In implementation, it merely means subtracting the elements of $\mathbf{G_{ab}}$ for each receiver's reference ray from all elements for that receiver (with the reference-ray elements of $\mathbf{G}$ becoming zero).

A useful aspect of DIT is the capability it affords to estimate statistical uncertainties in the tomographic reconstructions it produces. Our processor exploits this capability by including a program to compute the a-posteriori covariance matrix, as follows:

$$\widehat{\mathbf{V}} = \mathbf{G}^{-g} \mathbf{e} \mathbf{G}^{-gT} = \mathbf{v} - \mathbf{G}^{-g} \mathbf{G} \mathbf{v} \,,\tag{10}$$

and then transforming it to configuration space. This capability is illustrated for a WDLS case in which $\mathbf{G} = \mathbf{G_{ab}}$ in Figure 16 of Ref. 1.

2.1.2. Application of Theory

In applying the foregoing theory, two important considerations arise: the choice of basis functions and the weights to assign to them in defining the a-priori variance vectors, $\mathbf{v}$ and $\mathbf{e}$. The relative magnitudes of these two vectors determine the degree to which the processor treats the inversion as an overdetermined least-squares problem vs. that to which it produces the minimum-length solution, which would be a latitudinally uniform set of background profiles. The solution actually achieved is a weighted combination of the two. Substituting Eq. (7) into Eq. (5) produces

$$\widehat{\mathbf{m}} = \mathbf{G}^{-g} \mathbf{G} \mathbf{m} + \mathbf{G}^{-g} \mathbf{n} \,,\tag{11}$$

the second term of which indicates that the amount by which the estimated model vector, $\widehat{\mathbf{m}}$, differs from the true one, $\mathbf{m}$, includes an inverted combination of rms phase noise and model deficiency. The weight that the processor gives to each datum in solving the least-squares problem is dictated by the a-priori values assigned to the squares of these combinations, which are the elements of $\mathbf{e}$. Similarly, the weight given to estimating each model parameter is dictated by the a-priori values assigned to the elements of $\mathbf{v}$. (Since the a-priori expectation values of the $\mathbf{m}$ elements are zero, we also have the a-priori condition that $v_k = <m_k^2>$.) We have incorporated into our processor a capability for accepting interactively prompted user estimates of the relative magnitudes of $\mathbf{e}$ and $\mathbf{v}$ [the "damping parameter" described by Menke (1989)]. In most instances, the default weights described below should be appropriate.

Horizontal structures in ionospheric plasma density are dominated by large scales and are characterized approximately by a power-law spatial spectrum having an outer-scale cutoff, so we choose a Fourier representation for them. The set of harmonics employed is dictated by the image span and horizontal resolution available and by computational considerations regarding practicable matrix size. Our processor employs 60 harmonics. The estimated contribution of model deficiency to the a-priori estimates of **e** account mainly for ionospheric variance outside this finite spectrum.

For assigning a-priori weights to the elements of **v**, we assume a k^{-2} (one-dimensional) spatial spectrum with an outer-scale wavelength of five deg of latitude, along with eigenvalues emerging from a vertical EOF analysis of an ionospheric model. The model employed is that described by Secan (1980). In the present work, one objective was to identify a background profile and associated EOFs that would be broadly applicable. Accordingly, we performed the EOF analysis for the full range of latitudes (north and south) and longitudes, four GMTs (00, 06, 12, and 18 hrs), both solsticial (June) and equinoctial (March) conditions, and three sunspot numbers (20, 80, and 140). The background profile incorporated into our processor is the mean of 17,472 profiles spanning these conditions, our intent being that it represent an "all-time mean, generic ionosphere" to be perturbed by means of TEC data.

Initially, we expected to employ the EOFs spanning the foregoing broad conditions as vertical basis functions and their eigenvalues directly in evaluating the a-priori elements of **v**, but tomographic reconstructions obtained with such functions and a-priori coefficients were not consistently satisfactory. Becoming concerned about undue sensitivity to the basis functions used, we employed EOFs generated from more limited ranges of conditions (especially, geomagnetic latitude) to perform direct best fits to a test-case field of electron density (without attempting tomographic inversion of integrals through the fields). These test results are illustrated in Figures 1 through 4.

The top panel in Figure 1 contains contours of the logarithm of electron density derived from in-situ measurements at 800 km altitude aboard Satellite F8 of the Defense Meteorological Satellite Program (DMSP), extended vertically by means of a simple model profile. The bottom panel illustrates the best fit to those contours achievable with the eight EOFs generated in Phase I of this SBIR contract (hereinafter referred to as EOFs-1.8). The result was very satisfactory, with the only noticeable discrepancies being a modest excess of topside plasma and a bottomside gradient that is slightly too shallow. EOFs-1.8 were not derived specifically for the observing conditions of the DMSP-derived data set, but they had been tested previously against data from the same general latitude range.

Figure 2 contains the best fits achieved with our generic EOF set. For comparison with the other sets, we first employed eight functions (top panel). Subsequently we tested six generic EOFs (bottom panel). There is little difference between these contours and those shown in Figure 1 (bottom), especially in the top side. The bottomside gradient is shallower. As might be expected, the latter effect is exacerbated by decreasing the number of EOFs, but the resulting difference is less than that experienced in going from EOFs-1.8 to the generic set. It is pertinent to note that the contours are of $\log(N_e)$, not of N_e itself. Thus, differences in low-density regions (such as the extreme top and bottom sides) are accentuated.

5

Electron-density Field: Log (N_e)

Best Fit with EOFs-1.8: Log (N_e)
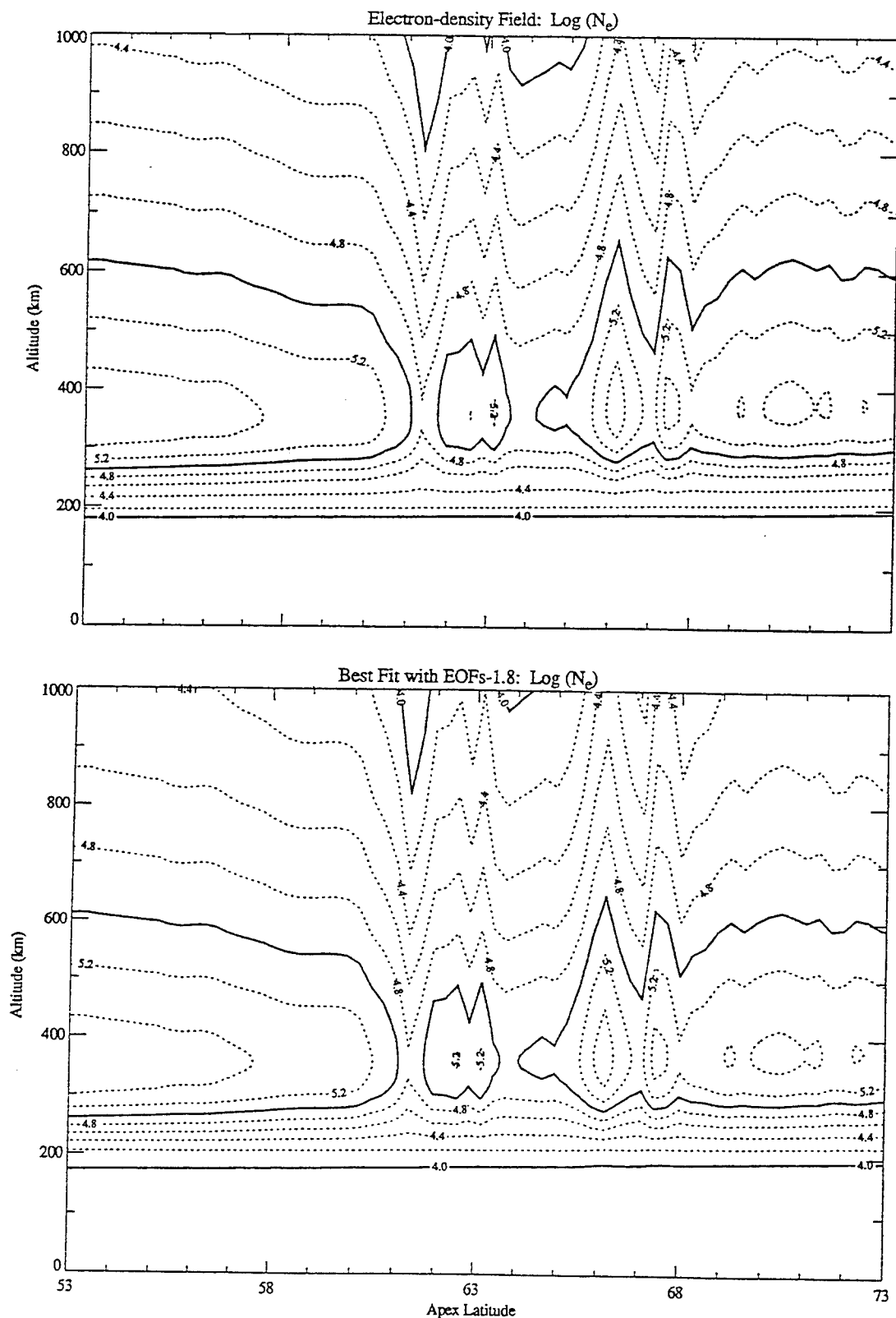
Figure 1. Illustrating profile mapping by means of EOFs. Top: contours of the logarithm of N_e (in el/m^3) derived from in-situ measurements aboard DMSP F8 (24 January 1990), extended vertically by means of a model profile. Bottom: best fit to top-panel contours achievable by means of eight EOFs generated in Phase I of this contract.

Best Fit with 8 Generic EOFs: Log (N_e)

Best Fit with 6 Generic EOFs: Log (N_e)
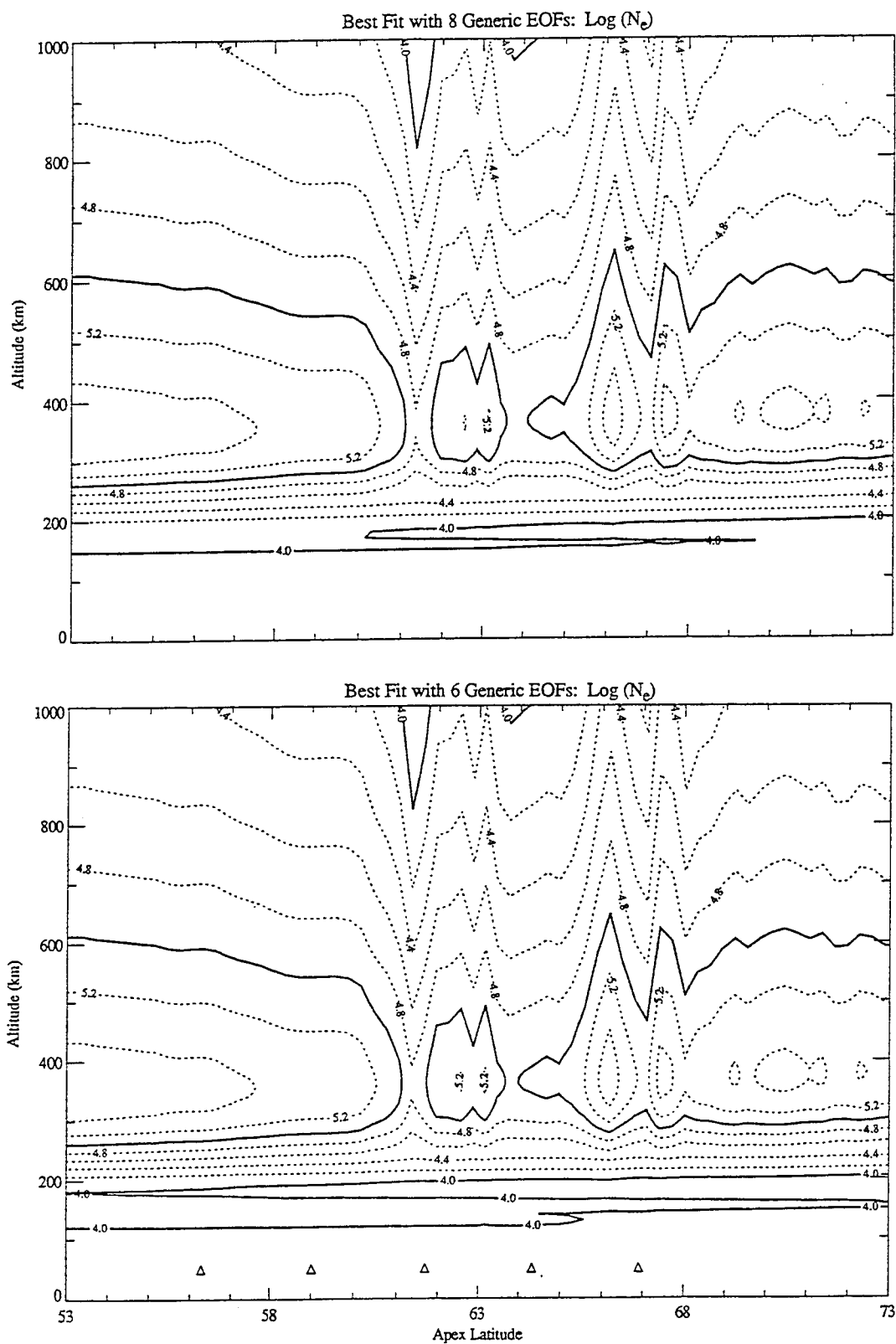
Figure 2. Best fits to Figure 1 (top) obtained with generic EOF set. Top: eight EOFs. Bottom: six EOFs.

7

Best fits with two additional EOF sets are shown in Figure 3. The top panel was obtained with eight EOFs generated from 6,552 profiles obtained by running the Secan (1980) model through the complete range of latitudes and longitudes, but for June only -- at 06, 12, and 18 GMT with sunspot numbers of 20, 120, and 220. The bottom panel was obtained from 8,418 profiles for the same conditions except that March profiles were added and that the latitude was limited to between 30 and 90 deg, thus excluding the equatorial region. Again there is little difference between these results and those from the other EOF sets, except in the low-density bottom side.

Fits with additional limitations appear in Figure 4. The top panel there shows results from EOFs-2.8, which were obtained from 6,552 profiles generated for June at GMT noon with sunspot numbers of 20, 120, and 220 (full range of latitudes and longitudes). The bottom one contains results from the most restricted set of conditions: namely, high-latitude winter. Its EOFs were generated from 1,095 profiles for June at 06, 12, and 18 hrs GMT for sunspot numbers of 20, 120, and 220, but with latitude restricted to between -60 and -90 deg (full range of longitudes). With this most restricted EOF set, the best-fit contours are remarkably similar to the original contours (Figure 1, top), even in the very low-density, extreme top and bottom sides.

We drew two conclusions from the foregoing tests, coupled with our initial lack of consistently satisfactory tomographic reconstructions. On the one hand, it appears likely that results could be improved by generating EOFs (and a background profile) for specific observing conditions (location, time of day, season, and solar-cycle epoch). On the other hand, the rather subtle differences between the foregoing results for different EOF sets (noticeable only in logarithmic contours through low-density regions) suggest no strong dependence on the EOFs themselves. We found our greatest limitation to lie, not in the choice of basis functions, but rather in the limited vertical resolution (due to finite grazing angle) achievable with surface-to-orbit geometry. As we shall see, this limitation manifests itself in a need for judicious choice of the a-priori weights to be applied to our generic EOFs.

Horizontal structures in our N_e test fields were reflected in our simulated TEC records via low-order vertical modes, but the limitation on vertical resolution prevented higher-order modes from restoring the relatively unchanged vertical profiles. Our solution was to impose a "zero-order" basis function proportional to the background profile. We then assigned a portion of the low-order variance contained in the eigenvalues obtained from the EOF analysis to this additional basis function when establishing the a-priori variance vector, v. This departure from the mathematical purity of strictly orthogonal basis functions permits accommodation of horizontal structures without distorting the vertical profile.

We have also introduced an additional ad-hoc vertical basis function. Our broadly based EOF analysis, the functions being empirical by definition, fails to isolate the E layer from the F layer. Since the layers do undergo somewhat distinct dynamic morphologies and since the foregoing zero-order function is heavily weighted in the F layer, it seemed prudent to introduce a separate function weighted mainly in the E layer. Such a function was, in fact, isolated in EOFs-3.8. We added it to our generic set, and again redistributed the a-priori variances, keeping the total variance (magnitude of v) equal to that obtained from the generic EOF analysis.

Best Fit with EOFs-4.8: Log (N$_e$)

Best Fit with EOFs-5.8: Log (N$_e$)
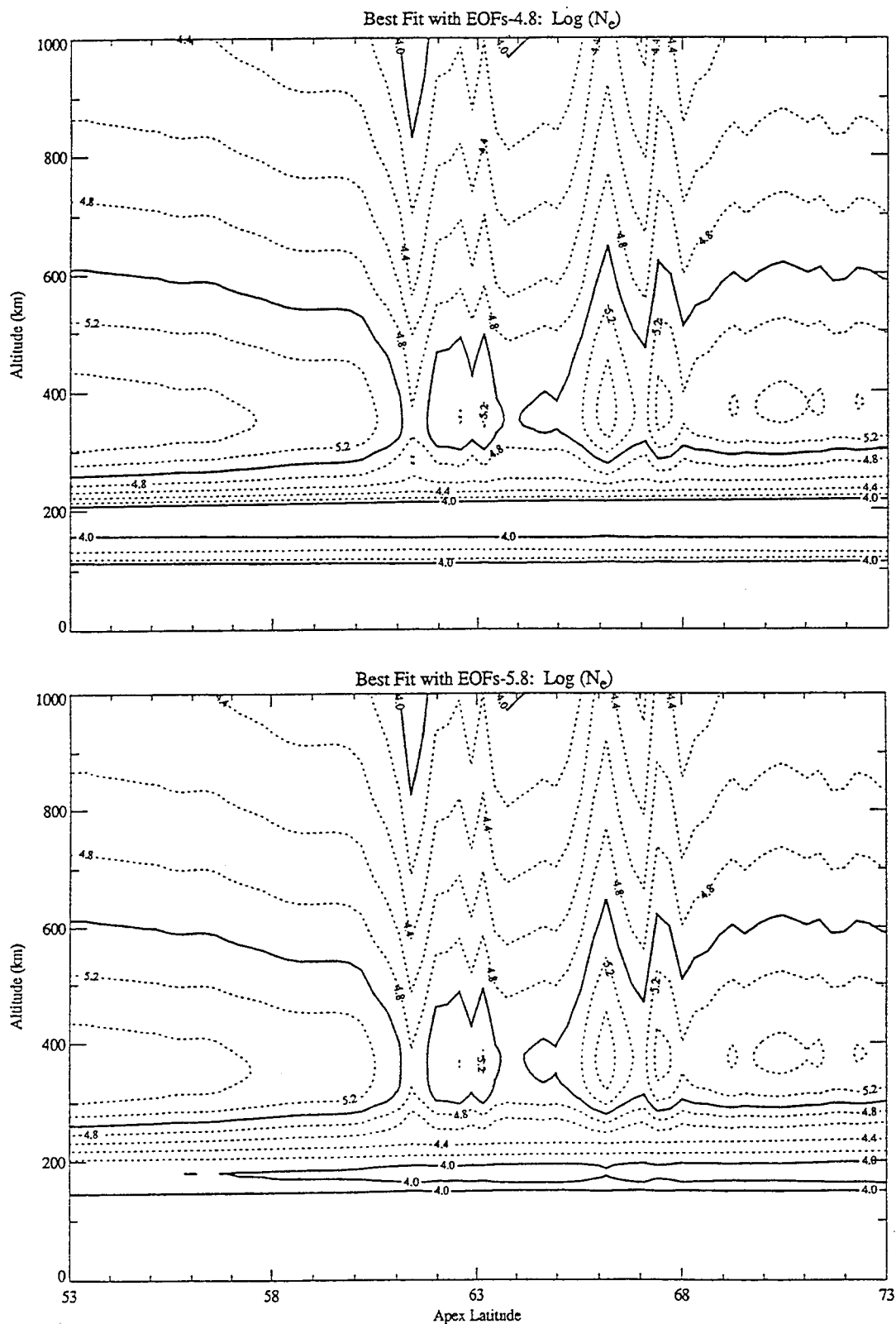
Figure 3. Best fits to Figure 1 (top) obtained with (top) EOFs-4.8, excluding equinoctial conditions and (bottom) EOFs-5.8, excluding equatorial profiles. (See text for complete description of conditions.)

9

Best Fit with EOFs-2.8: Log (N$_e$)

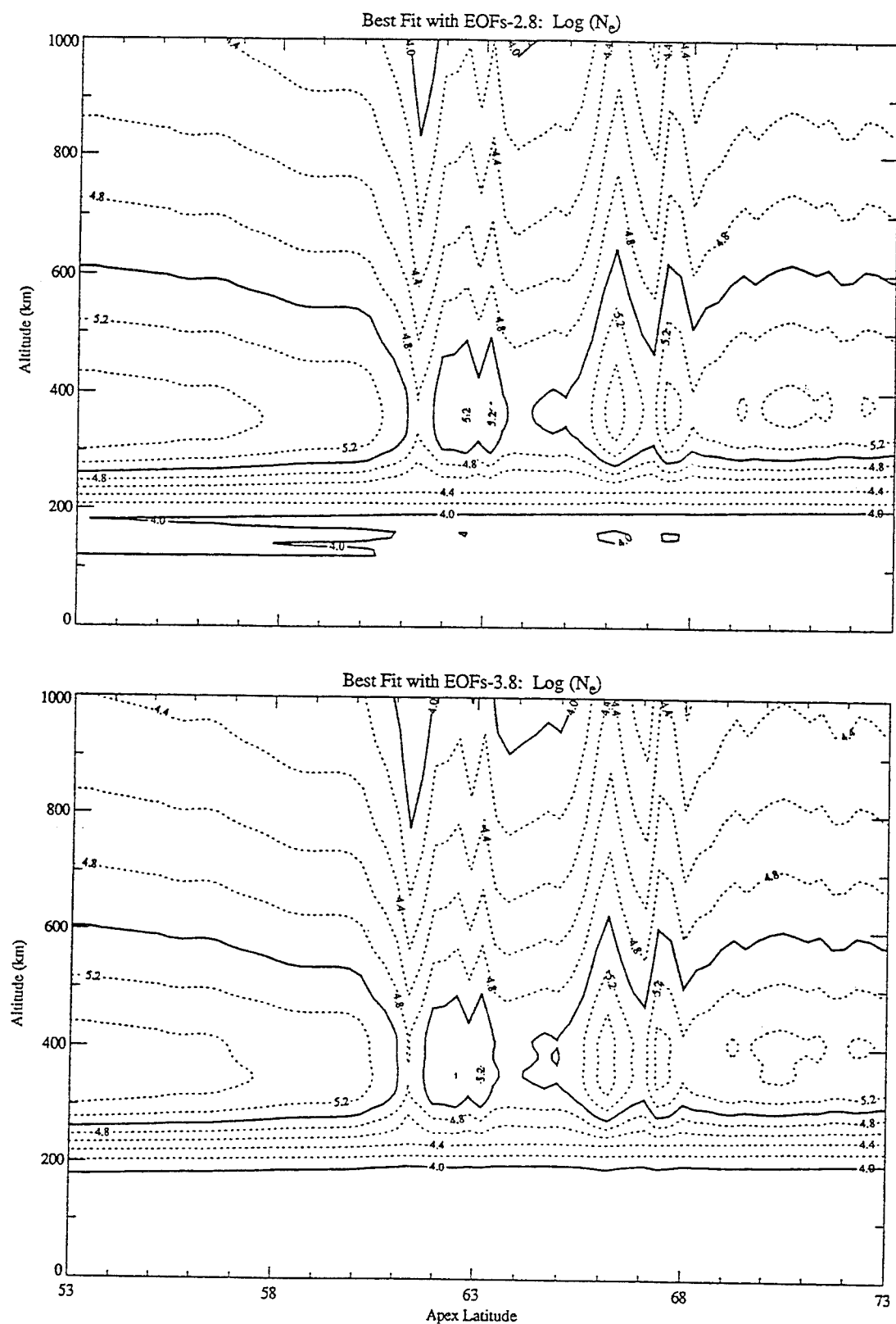Best Fit with EOFs-3.8: Log (N$_e$)

Figure 4. Best fits to Figure 1 (top) obtained with (top) EOFs-2.8, excluding equinoctial conditions and limited to a single GMT and with (bottom) EOFs-3.8, generated from high-latitude, winter profiles only.

The combined set of vertical basis functions in our central processor is depicted in Figure 5. The solid curves represent EOFs 1 through 4 from the broadly based analysis. The dashed curve is the "zero-order" function derived from (proportional to) the generic background profile, and the dotted one is that added to represent the E layer. In our processor, the latter is employed as the last of six vertical basis functions identified as of order 0 through 5. They are taken to account respectively for 78.3, 11.0, 7.3, 2.3, 0.6, and 0.5 % of the a-priori variance about our generic background profile. For each vertical function, its share of the a-priori variance is taken to reside half in case-to-case ("temporal") variations and the other half in the k^{-2} spatial spectrum described above. The spatially dc term, since it is applied independently to each vertical function, permits latitudinally uniform variations in the profile, just as the zero-order vertical function accommodates vertically uniform horizontal structures.

2.2   Spatial Resolution

A standard way to assess the spatial resolution achievable with the ITS processor is to investigate its impulse response. One way to do this is to expand a two-dimensional delta-function perturbation in the model basis functions and then to multiply the result by the model resolution matrix, $\mathbf{R} = \mathbf{G}\mathbf{G}^{-g}$. Doing so produces the basis-function expansion of the resolved perturbation, since we have from Eq. (11) that, in the absence of noise, $\hat{\mathbf{m}} = \mathbf{Rm}$. This result, when mapped back to configuration space, can be compared with the true perturbation function. We have done so, approximating a delta-function perturbation by means of a narrow gaussian and employing the EOFs shown in Figure 5 as our vertical basis functions (along with our 60 horizontal harmonics).

As an intermediate step, we also have mapped the basis-function expansion of the gaussian itself back to configuration space. This provides an assessment of the best that can be done with the basis set we're using, analogous to the best fits performed in producing Figures 1 through 4. Defining the $\mathbf{G}$ and $\mathbf{G}^{-g}$ matrices for five equally spaced receivers spanning from 58 to 68 deg latitude, we placed our test perturbation, which had half-peak gaussian diameters of 1.2 deg horizontal and 58.9 km vertical and a peak plasma density of 10^{12} el/m^3, at 350 km altitude and 63 deg latitude. We refer below to it as the "true" perturbation, to the remapped basis-function expansion as the "projected" perturbation, and to the remapped result after multiplying by $\mathbf{R}$ as the "resolved" perturbation.

Figure 6 shows the true (solid) and the projected (dotted) perturbations (with the latter renormalized to the original peak perturbation), along with the resolved (dashed) perturbations for two cases. The cases were defined by minimum-elevation masks (five and 15 deg) that produced different numbers of raypaths (1320 and 1026, respectively). The most obvious result is that the projected curve is substantially broader vertically than the true one, indicating that the vertical resolution of the prototype ITS is limited to about 140 km half-peak gaussian diameter. Note also that the upper radius is larger than the lower one. A similar test with the perturbation placed at 500 km altitude disclosed smearing essentially throughout the topside F layer.
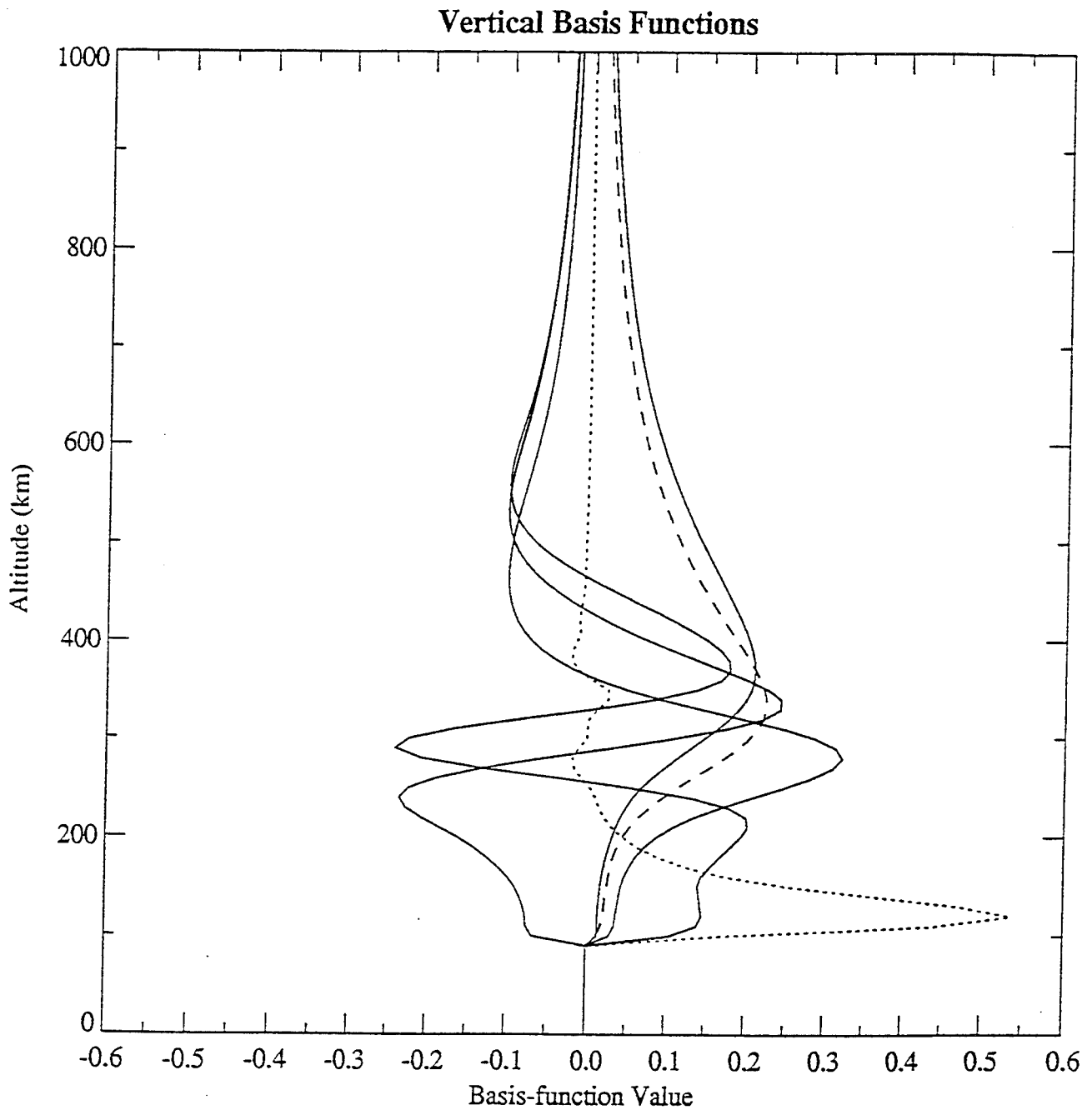
11

Vertical Basis Functions

Figure 5. Vertical basis functions employed in the NWRA ITS central processor. Solid curves depict four EOFs derived from 17,472 disparate ionospheric profiles. Dashed curve denotes a "zero-order" basis function proportional to the mean of those profiles. Dotted curve demarks a basis function heavily weighted in the E layer.
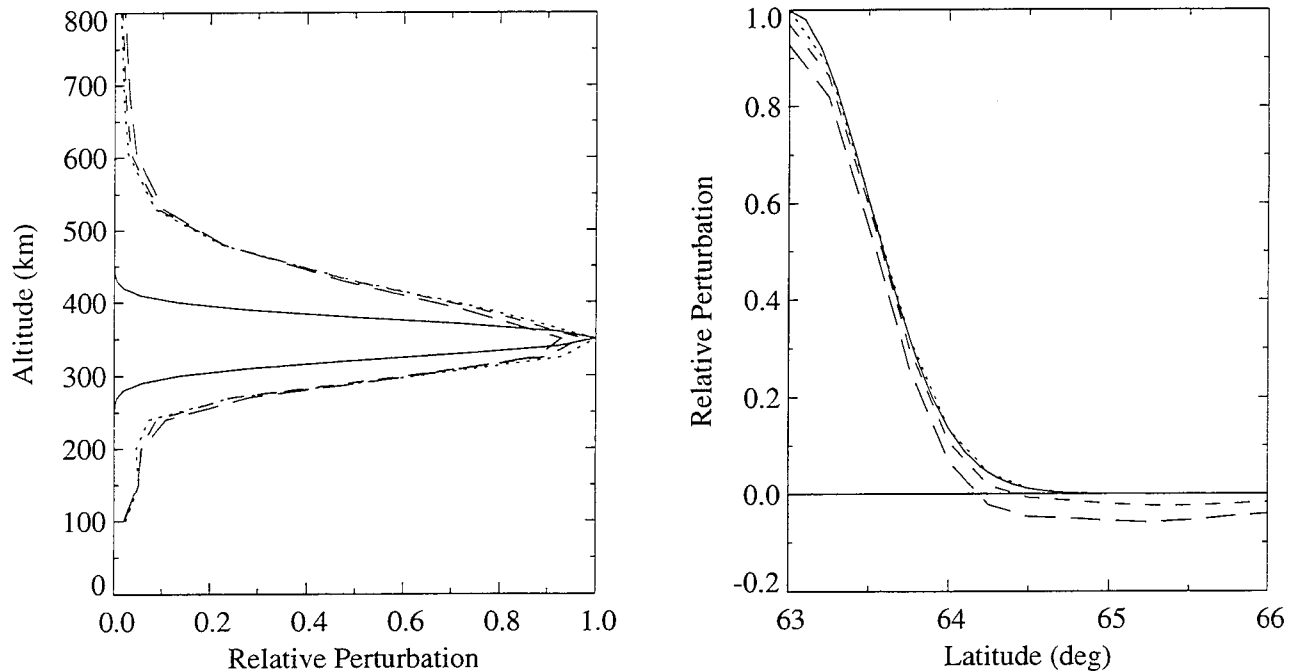
Figure 6. Vertical (left) and horizontal (right) true (solid), projected (dotted), and resolved (dashed) perturbations. There are two resolved perturbations, one (long dash) corresponding to a 15-deg elevation mask, reaching a peak of 92% of true, and one (short dash) corresponding to a 5-deg mask, reaching a peak of 97%.

Interestingly, the two resolved perturbations are not noticeably broader than the projected one. Thus, at least for Gaussian-shaped features, vertical resolution appears to be limited more by our EOF set than by the geometry contained in G and G^{-g}. This holds promise for improvement through use of higher-order EOFs, given a refined means for a-priori weighting or reduced coupling between vertical-mode dependence on that weighting. (We'll return briefly to the latter possibility in Section 5.) One also must take note, however, that a gaussian test perturbation is itself of limited utility. Even though it is a common standard for defining resolution, one should not be too surprised that it is not well represented by basis functions chosen empirically for efficient representation of the ionosphere.

Horizontally, all the perturbations have about the same width. This indicates that the prototype ITS can resolve features with half-peak gaussian diameters of about a deg (100 km at 350 km altitude), and probably smaller. We did not investigate finer resolution so as not to overstate capabilities, given that our processor employs straight-line (as opposed to ray-trace) propagation.

While the most obvious characteristic of Figure 6 is the difference between the true and projected gaussians vertically, it is pertinent also to note smaller differences between the two resolved gaussians. They both fall slightly short of the peak density in the original perturbation and go slightly negative in their horizontal cuts, but both these behaviors are more pronounced in the curves generated with a 15-deg elevation mask (long dashes) than in those generated with a five-deg mask (short dashes). That is, adding more nearly horizontal rays helps, a point to which we shall return in Section 2.4. The degree to which it helps may be quantified by noting the improvement in resolving of

13

a-priori plasma-density uncertainty, an improvement shared by all the vertical modes, as displayed in Table 1. The a-posteriori spatially averaged rms uncertainty is reduced from 37 per cent to 13 per cent (the variance from 14 per cent to 2 per cent). This is due to having more data (albeit with larger noise), as well as a better sampling from the point of view of geometry. The underprediction of peak amplitude and the negative tails result from the large perturbation relative to expectation (5.8 times the a-priori rms) and the fact that only relative TEC is measured.

Table 1. Percent of a-priori Variance Resolved

EOF	15-deg Mask	5-deg Mask
1	60	70
2	47	56
3	53	80
4	44	77
5	43	72

2.3. The Programs

We have committed the theory described in Section 2.1.1 and the function and parameter choices discussed in Section 2.1.2 to four of the six programs that constitute the NWRA ITS central processor, namely 'g_mtrx', 'g_invrt', 'ion_image', and 'stat_comp'. The other two programs are named 'create_pass' and 'prep_dat'. All significant computation time is consumed in 'g_mtrx', which computes the geometry matrix, G, and 'g_invrt', which inverts it to produce G^{-g}. They and 'create_pass' may be run at any convenient time after satellite ephemeris information is in hand for the epoch of a particular pass, as may 'stat_comp'. The latter is optional, being required only if the user desires information about statistical uncertainties in the tomographic reconstruction to be produced, as described in the final paragraph of Section 2.1.1 and illustrated in Figure 16 of Ref. 1. Only 'prep_dat' and 'ion_image', which can be run in a matter of seconds on a modest work station, require that dispersive-phase data from the pass be in hand. We describe the programs, in the order in which they are likely to be employed by a user, in a separate compendium of computer programs (Fremouw, 1994), following the format prescribed on AFSC Form 1546.

2.4. Simulated Results

We have tested our processor primarily be means of actual data from the in-situ plasma-density sensors flown on DMSP, such as those used for the top panel in Figure 1. To obtain such test data, we first extended horizontal (essentially latitudinal) records taken near 800 km altitude vertically by means of representative model profiles (Secan, 1985). These "true" profiles were derived by means totally independent of the model used to generate our background profile and EOFs, stemming from a combination of other published models. Specifically, we used the model by Bent et al (1976) to describe the shape of the F layer near its peak, with its density and height initialized respectively by means of the CCIR model (Rush et al, 1989) and a prescription by Jones et al (1969). Below the F-layer peak, we employed the Air Weather Service RBTEC model (Flattery and Ramsay, 1976). The topside profile shape was described by means of a simple two-component (O^+ and H^+) diffusive-equilibrium model. Once initialized, the thickness and peak density of the F

14

layer were adjusted iteratively to match the in-situ density measured at each profile latitude by means of DMSP. Similarities between the "true" profile and the a-priori background profile stem solely from the fact that both are based on (independent) models intended to describe the actual F layer.

To obtain simulated TEC data, we integrated through the two-dimensional fields of "true" electron density. Such simulated records derived from the in-situ data used for Figure 1, taken by means of the Special Sensor for Ions, Electrons, and Scintillation (SSIES) on board DMSP F8 on 24 January 1990, appear in Figure 7 for five hypothetical TEC receiving stations located between 58 and 68 deg north latitude. (Our processor operates in geomagnetic latitude, treating plasma density as constant in geomagnetic longitude, but we used geomagnetic and geographic coordinates interchangeably in our tests.)

The processor employs all available rays above ten deg elevation that penetrate the ionosphere above 100 km altitude at geomagnetic latitudes two deg north and south of the northernmost and southernmost receiving stations. Figure 8 presents results for a simulated pass using data from above our ten-deg elevation mask (so that the processor used only the solid portions of the curves in Figure 7). The upper panel shows the "true" electron-density field derived from the DMSP data (same as top panel in Figure 1, recast as contours of N_e rather than its logarithm), and the lower panel shows the tomographic reconstruction obtained. The processor generated the geometry matrix for this case in 8 min 35 sec on a Sun SPARCstation 10 Model 30 with 64 Mbytes of memory and inverted the matrix in 9 min 27 sec. (Neither of these operations requires the data to be in hand; they may be performed at any convenient time after the appropriate satellite ephemeris is available.) Multiplying the inverted matrix by the data and transforming the result to configuration space to produce the image shown in the lower panel took 11 sec on the same machine (All times include interaction with a UNIX script.)

In Figure 8, horizontal structures on scales down to somewhat less than one deg of latitude (about 100 km in extent) are reproduced rather well. (The wavelength of the highest harmonic employed for all inversions illustrated in this report was 0.67 deg, unless otherwise noted.) Smaller structures are not fully resolved. For instance, the reconstructed 1.0×10^{11} el/m^3 contour is barely broken near 61 deg latitude and is not broken at all near 64 deg latitude, whereas the "true" contour is completely pinched off in both places.

Vertical rendering is less satisfactory, the entire reconstructed layer being somewhat too low and the bottomside gradient too shallow. Note, for instance, that the first contour lies slightly below 200 km in the lower panel, while it is decidedly above 200 km in the upper one. To identify the effect of improved vertical resolution by retaining lower-elevation (and, therefore, lower-grazing-angle) rays, as noted in Section 2.2, we ran this case with a lower elevation mask, namely five deg. This result, obtained using the longer TEC curves in Figure 7, is shown in the lower panel of Figure 9. There is modest vertical improvement, with the first contour on the bottomside now being slightly above 200 km and the vertical placement of most other contours being improved as well.

Interestingly, the additional rays have improved the horizontal resolution also. The 1.0×10^{11} contour now breaks essentially where it should. There also have been minor losses, however, such as the foreshortening of the 2.0 contour equatorward of the main ion trough and disappearance of the two 1.5 contours in the resolved feature near the center of the plot. Moreover, the additional rays substantially increased run time. Now generating the matrix took 31 min 21 sec, and inverting it took 49 min 21 sec. Generating the image from the data took 27 sec. In the next
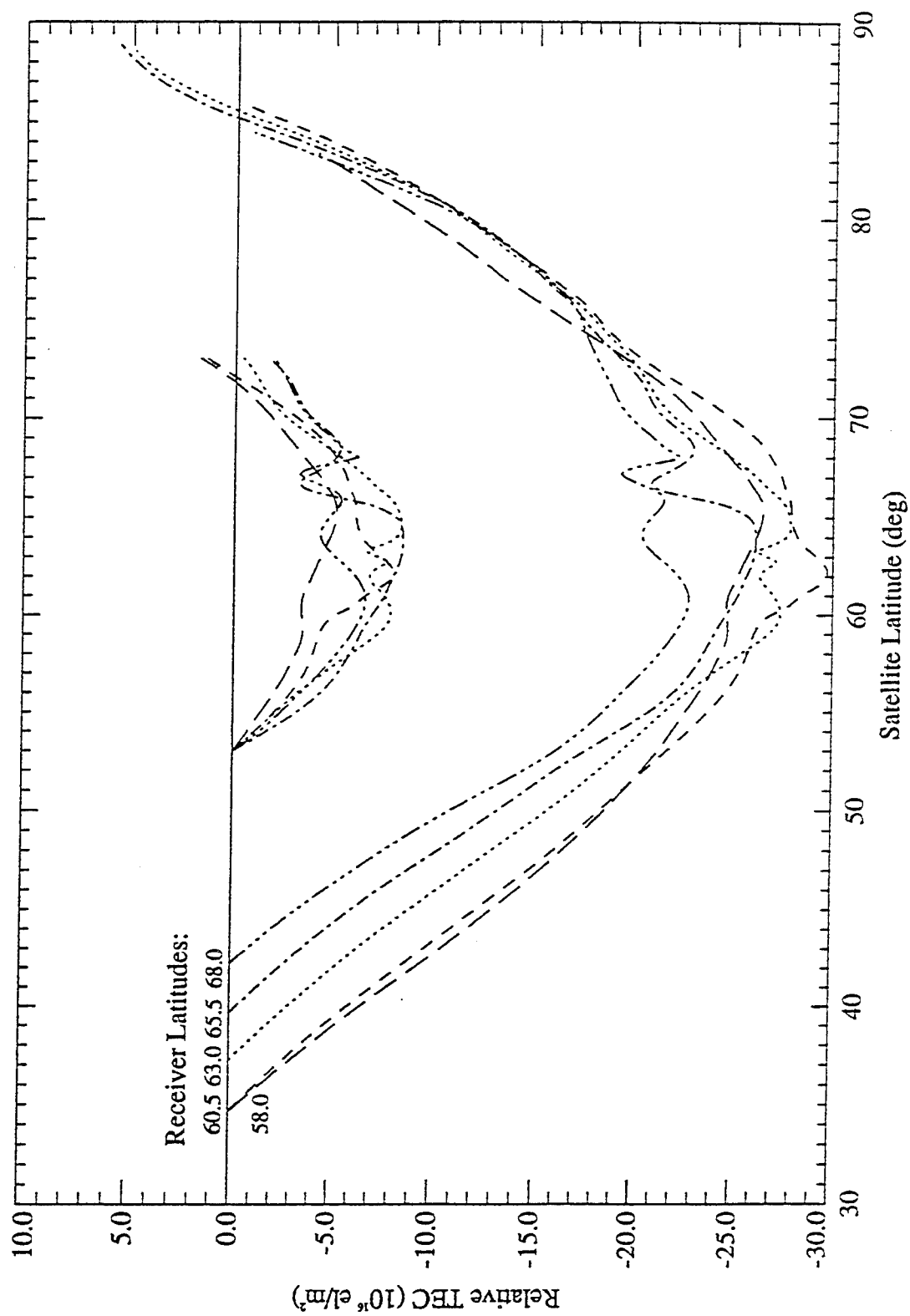
15

Figure 7. Simulated TEC records for five hypothetical receiving stations, derived from SSIES records of plasma density recorded on DMSP F8 on 24 January 1990. Short curves employed in first test discussed; long ones employed in second test.

16

Electron-density Field: N_e (10^{11} el/m^3)

Tomographic Reconstruction: N_e (10^{11} el/m^3)

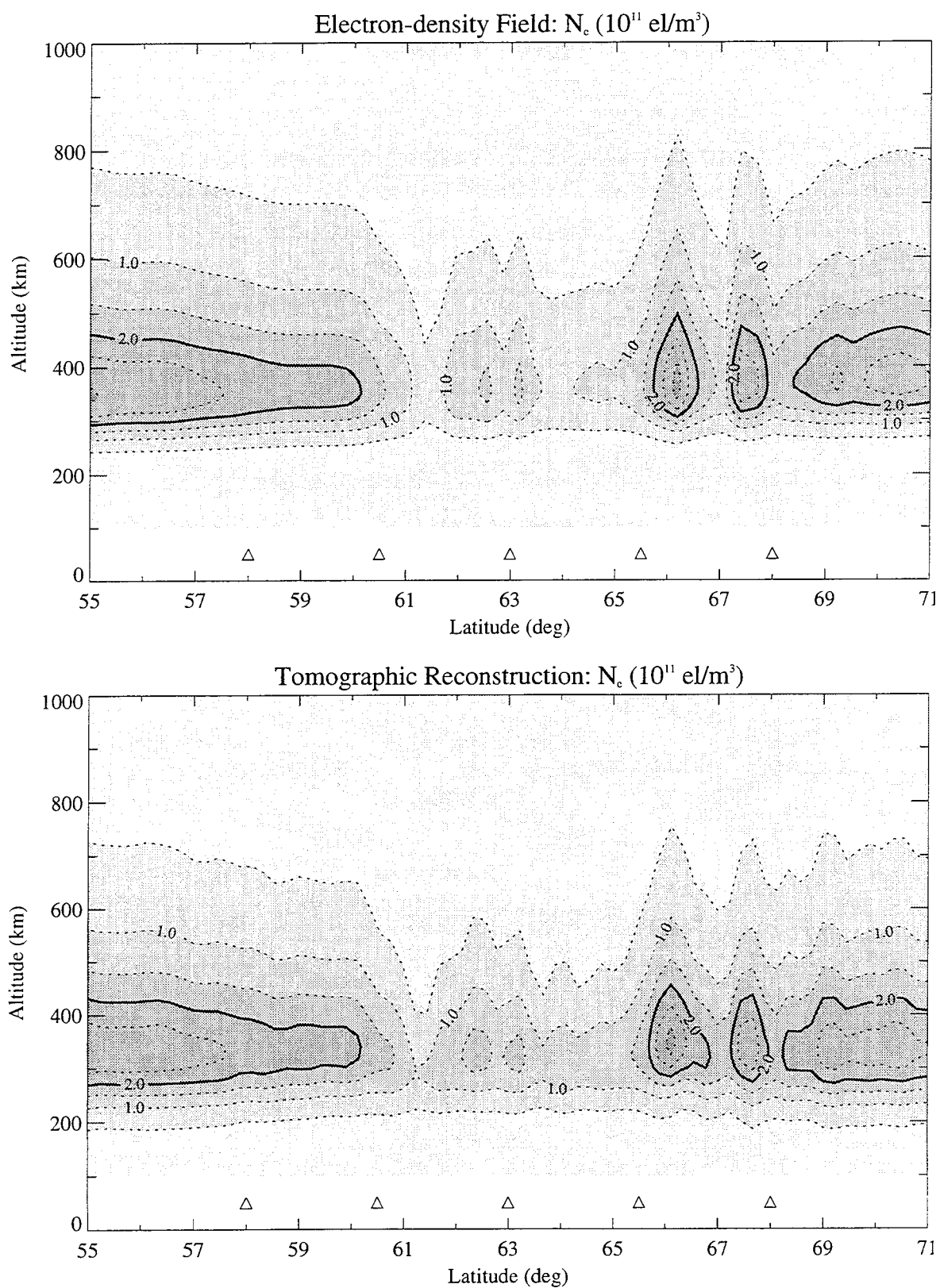Figure 8. Simulated results. Top: "true" electron-density field derived from DMSP in-situ data. Bottom: tomographic reconstruction obtained using short simulated TEC records shown in Figure 7. Triangles above ordinate demark receiver locations.
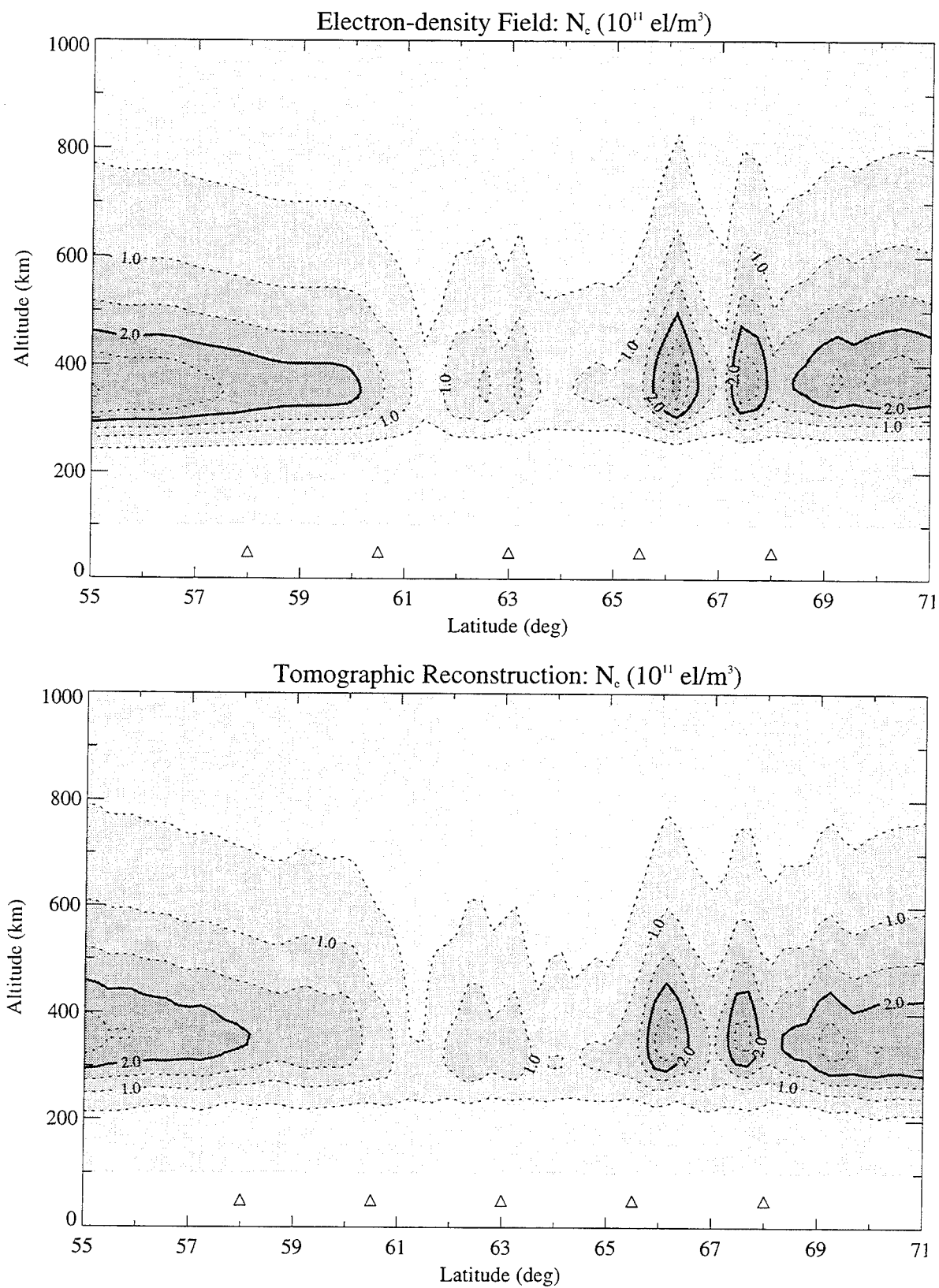
Figure 9. Simulated results. Top: same as upper panel of Figure 8. Bottom: tomographic reconstruction obtained using longer simulated TEC records shown in Figure 7.

two cases, we'll use only rays above our processor's ten-deg elevation mask. For them, the run time was similar to (slightly shorter than) that quoted above for the case in Figure 8.

In Figure 10, we present results from a higher-density case than the foregoing, having somewhat less prominent horizontal structures in the trough region and the auroral F layer. Again, the "true" electron-density field is displayed in the upper panel and the tomographic result in the lower one. The gray scale is the same in the present case as in the preceding (and succeeding) one, to facilitate comparison of absolute densities. Here the mid-latitude F layer reaches a peak density between 6.5×10^{11} and 7.0×10^{11} el/m^3, a fact reproduced in the tomographic reconstruction. The reconstruction places the equatorward wall of the main trough (closing of the 4.0×10^{11} contour) quite accurately near 62.4 deg latitude. All major horizontal structures are reproduced, although their peak densities are slightly underestimated. That the peak density is estimated within 0.5×10^{11} el/m^3 (somewhat more closely if finer contours are plotted) does indicate a reasonable level of success in dealing with the $2n\pi$ ambiguity. Vertical resolution again is less satisfactory, with the layer being too low and the bottomside gradient too shallow.

Figure 11 contains results from a case combining the greater density range of Figure 10 with the more prominent horizontal structure of Figures 8 and 9. They are quite consistent with the forgoing cases, with horizontal resolution being superior to vertical rendering and with peak density being underestimated by about 5×10^{10} el/m^3 (8 %).

In Figure 12, we present the somewhat simpler case sent to us "blind" by the Contracting Officer's Technical Representative during Phase I of this project, containing a single auroral F-layer "blob" poleward of the main trough. The original contours appear in the paper by Raymund et al (1990), and renderings of it with our absolute-TEC processor are contained in Figures 9 through 13 of Ref. 1. That processor employed (a different set of) eight EOFs and 30 harmonics. In Phase II, we have found that investing computer time in generating and inverting matrix elements pertaining to more than about six EOFs is not cost-effective, due to the limited vertical resolution available inherently from surface-to-orbit viewing geometry. Investing in higher harmonics is productive, however, to control ringing when resolving sharp horizontal gradients such as that in the present case. In this case, the wavelength of the highest harmonic was 0.60 deg of latitude (about 60 km).

Comparison of Figure 12 with the original contours reveals the following characteristics of this case. As with the other cases, horizontal rendition is quite good, with placement of major features (trough and "blob") being accurate within 0.2 deg (about 20 km), which is the size of a plot resolution cell. Compared with our earlier processor, vertical rendering and resolution are somewhat improved. The bottomside contours (starting with 4×10^{10} el/m^3, the lowest one in the original field) for the most part are placed appropriately within a resolution cell (20 km) or so. The topside gradient is improved, but still somewhat shallower than the original. The F-layer peak is about 20 km (one resolution cell) too high, but its tilt (increasing height with increasing latitude) has been rendered quite well with five stations spanning 7.3 deg of latitude. The estimate of peak density is about 5×10^{10} el/m^3 too low, whereas that of our previous processor was about 4×10^{10} too high. Thus, we have not lost much in terms of ambiguity resolution in going from an absolute-TEC processor to one that operates directly with relative TEC data.

The results illustrated in Figures 8 through 12 represent tests of Programs 'g_mtrx', g_invrt, and 'ion_image'. No multi-receiver data exist for testing Program 'prep_dat'. Single-receiver data

Figure 10. Simulated results. Top: "true" electron-density field derived from in-situ data collected on board DMSP F8 on 27 August 1991. Bottom: tomographic reconstruction of "true" field.

Electron-density Field: N_e (10^{11} el/m^3)

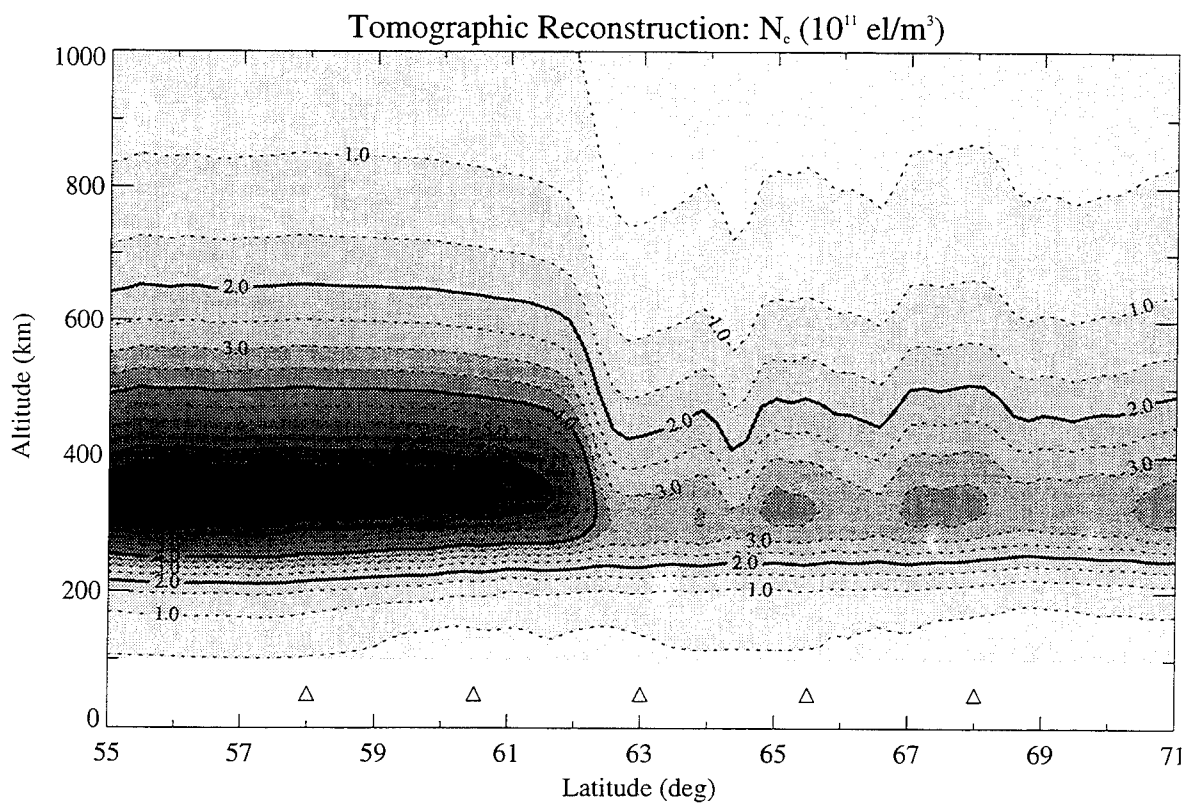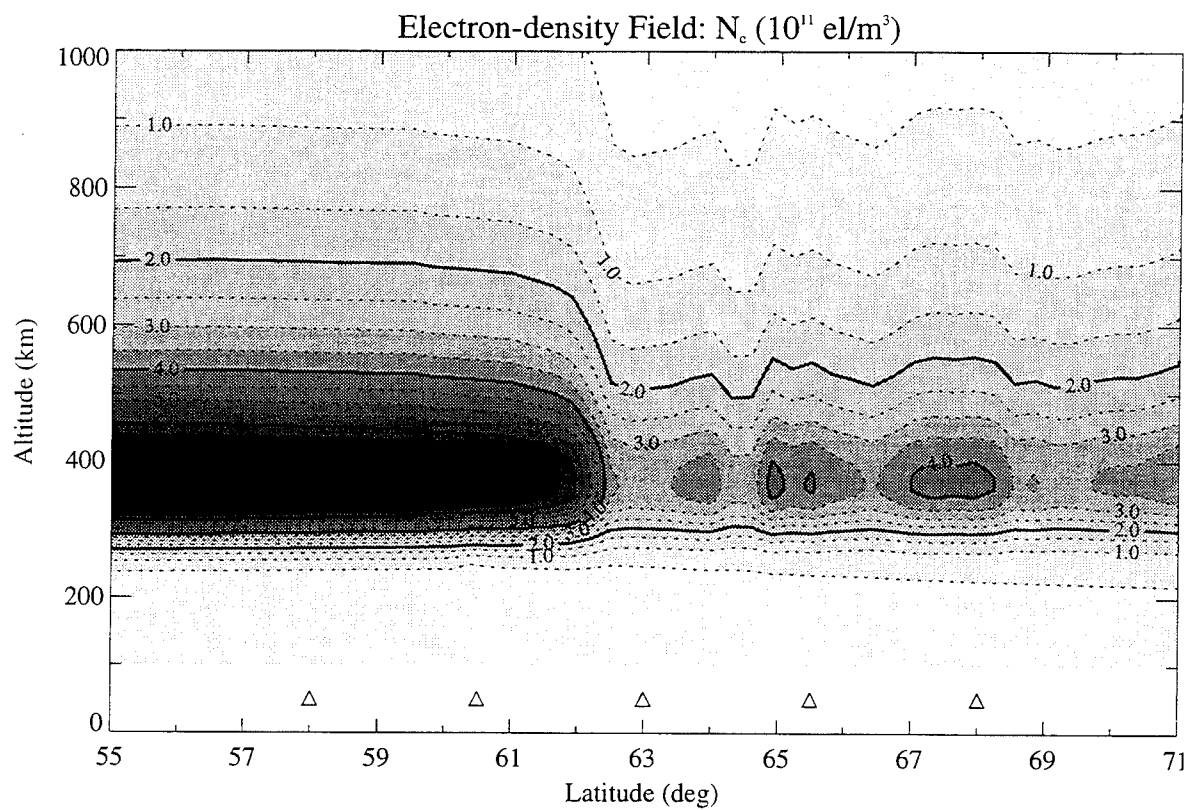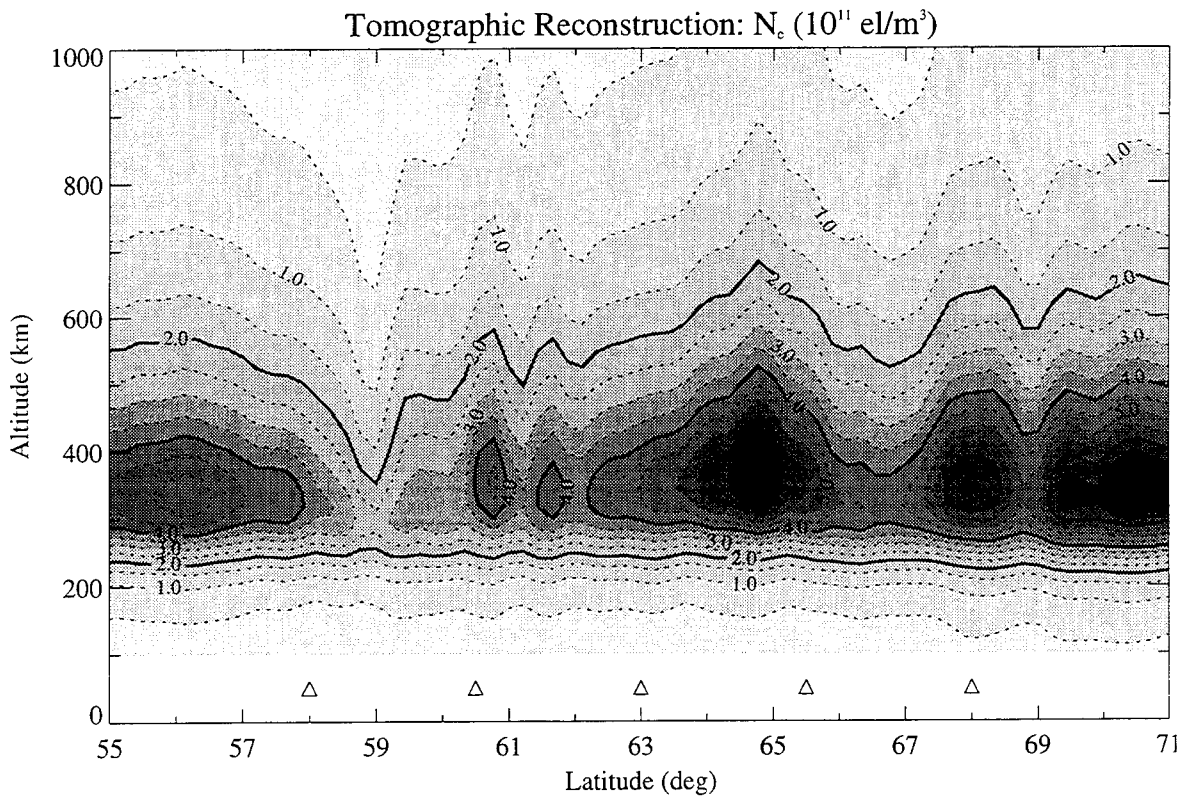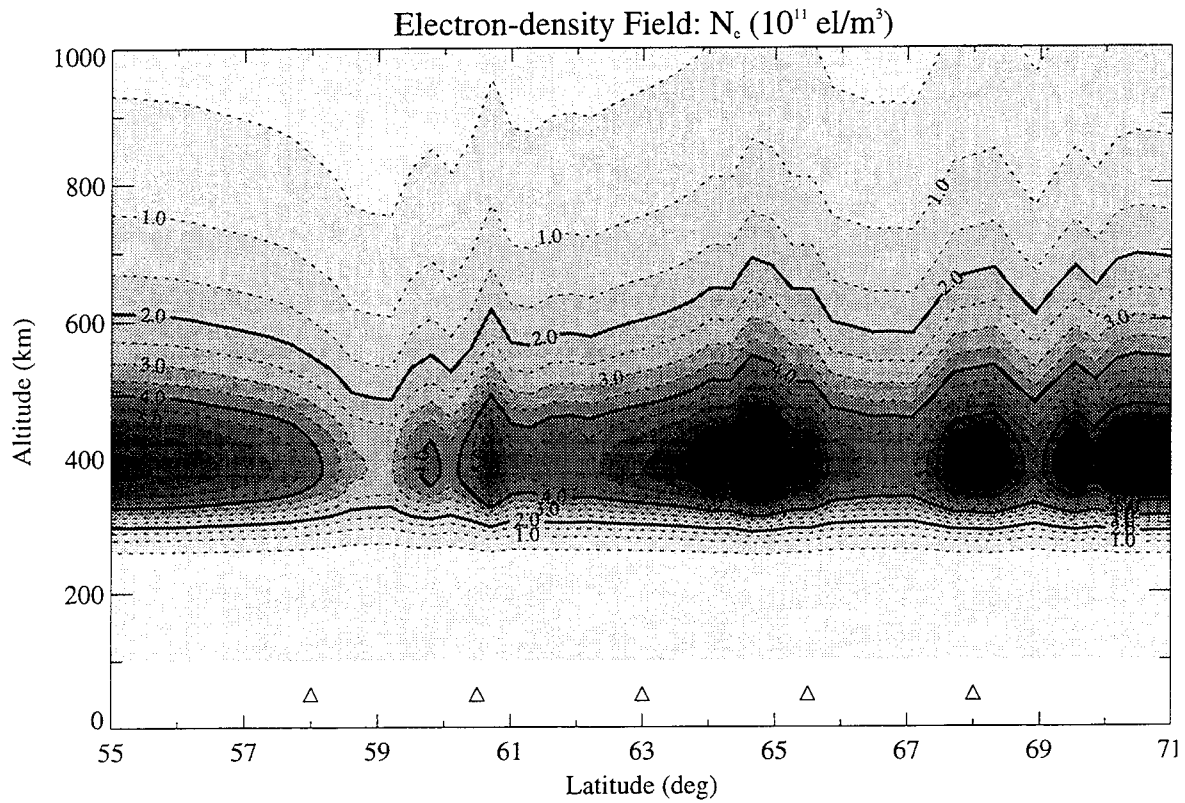## Tomographic Reconstruction: N_e (10^{11} el/m^3)

Figure 11. Simulated results. Top: "true" electron-density field derived from in-situ data collected on board DMSP F9 on 27 August 1991. Bottom: tomographic reconstruction of "true" field.

21

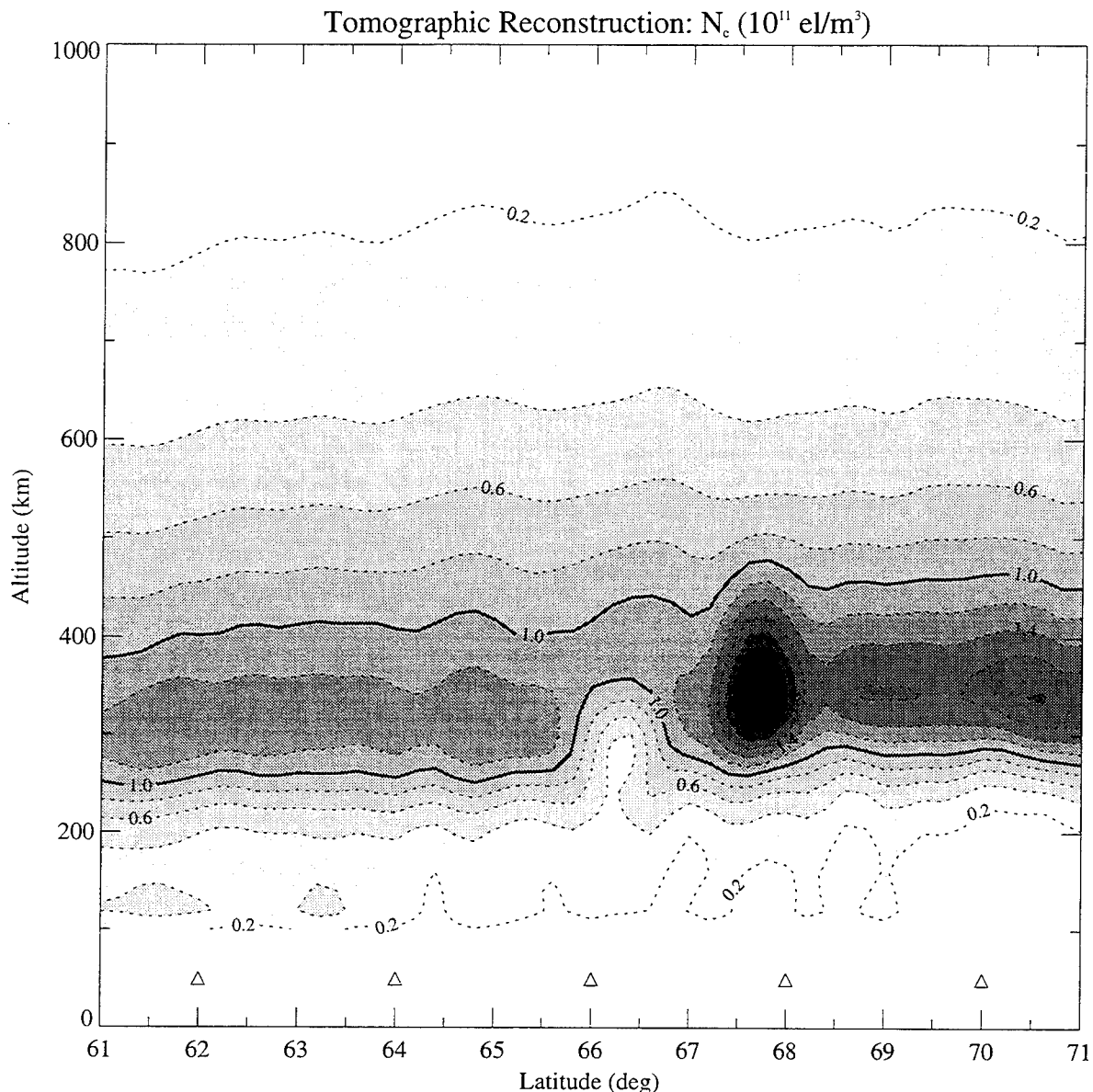**Tomographic Reconstruction: N_c (10^{11} el/m^3)**

Figure 12. Simulated results from a case presented to us "blind." For original contours, see Figure 6 of paper by Raymund et al (1990); for renderings by our absolute-TEC processor from Phase I, see Ref. 1.

from an NWRA ITS10S receiver that operated briefly at Thule, Greenland, are available, however. We employed such data for testing 'prep_dat', simulating additional stations by shifting the same records in time. We ran 'create_pass' for a fictitious five-receiver chain in the Arctic, including Thule as its central station, to produce a 'pass_info' file to be read by 'prep_dat'. To test the editing capabilities of the latter, we selected an actual pass displaying scintillation activity and data dropouts. The resulting 'see_dat' and 'see_tec' files and the editing information provided by the program are illustrated in separate documentation of computer programs (Fremouw, 1994), along with similar information from tests of 'create_pass', 'stat_comp', and the other programs.

3.   THE ITS10S DATA-COLLECTION SUBSYSTEM

In Ref. 1, we described a baseline design for a fully digital coherent receiver for collecting dispersive-phase data from the Transit satellites. As a cost-saving measure, our Phase-II proposal (Fremouw, 1990) described development of a less expensive receiver employing an analogue signal processor. In a separate proposal (Fremouw and Lansinger, 1991), aimed at diagnosis of plasma-density structures produced in the ionosphere by means of radio-frequency heating, we described an enhanced digital receiver for recording ionospherically produced radiowave scintillation as well as dispersive phase. The objective underlying the latter proposal was augmentation of the ITS with scintillation capability at a reasonable incremental cost.

The latter proposal, submitted under the joint-services High-frequency Active Auroral Research Program (HAARP) was declined. Upon initiating our SBIR Phase-II design work, however, we conceived a compromise that retained the flexibility needed for subsequent augmentation without incurring all the development costs of the baseline, fully digital receiver. In the baseline receiver, carrier synchronization would have been achieved in the digital signal processor (DSP). The compromise constituted a hybrid approach in which synchronization is carried out in an analog phase-locked loop (PLL) of familiar design and consequently reduced engineering cost while still retaining the option for subsequent scintillation enhancement by means of a DSP. The hybrid design resulted in a receiver, designated the NWRA ITS10, with a capability to record VHF intensity scintillation and a potential for subsequent addition of a similar UHF capability at modest cost.

During our Phase-II work, we received a sufficient number of inquiries from potential DoD and non-DoD users of an augmented receiver that we carried out the design augmentation as an Internal Research and Development (IR&D) project. The augmented instrument became known as the NWRA ITS10S coherent receiver. In addition to recording dispersive phase at a sample rate sufficient for TEC tomography, it records scintillations in phase and both VHF and UHF intensity, each at 50 sps. It is now available as a commercial product (as is the ITS10). Initial sales (of the 10S) have been made to USAF and to Moritani America, Inc., the latter for export resale to the Japanese government's Communications Research Laboratory. Based on the IR&D design, we proposed (Fremouw, 1993) conversion of the ITS10 receivers built for the prototype ITS to ITS10S capability. That proposal was funded as an add-on to this contract, and the prototype data-collection subsystem includes five ITS10S receivers. The ITS10S is described fully in an R&D Equipment Information Report (Lansinger et al, 1994).

4.   THE DATA-RETRIEVAL SUBSYSTEM

When an ITS10S receiver and its associated PC are installed at a manned station, data retrieval can be as simple as downloading the raw and/or PC-processed data from hard disk to diskette. Alternatively, data files may be retrieved from any station with standard telephone service by means of a modem. For ease of installation in the prototype ITS, an external modem is being delivered with each PC. The Hayes[R]-compatible modems being delivered, Model PM14400FXMT V.32bis from Practical Peripherals[R], operate at up to 14.4 kbaud and come bundled with Quick Link II[TM] Data/Fax software. Complete hardware and software documentation is provided with each modem.

In the event that one or more of the receiving stations in an ITS chain is located at a site lacking standard telephone service, data may be retrieved by means of relay through GOES. A GOES DCP is being delivered with the prototype ITS for relay of data from a single ITS station. For relay-

ing data from multiple remote stations, assuming no local telephone service for modem connection between stations, diskettes could be carried to the one station outfitted with the DCP delivered. Alternatively, additional DCPs could be purchased commercially.

The DCP being delivered is of the 3400 Series from Synergetics International, including a 3401B master control module, a 3489A power supply, a 3421A GOES transmitter with an associated Model 18B crossed Yagi antenna, a 3435A interface module with an RS-232C input cable, and complete 3400-Series documentation. When properly installed with data flowing from the station PC to the interface module, the DCP will send PC-processed data via its UHF transmitter to GOES, which will relay the data via its S-band transponder to Wallops Station, VA. Once stored in identified user queues at Camp Springs, MD, the data are available 'round the clock over the next 72 hours for user retrieval via modem.

Our DCP has been classified as a "self-timed" one by the National Environmental Satellite, Data, and Information Service (NESDIS) of the National Oceanic and Atmospheric Administration (NOAA), which operates and controls GOES. For purposes of developmental testing, we were identified by the User ID "NWREAS" and assigned address 9800032E on Channel 037 East (401.7550 MHz). The address authorized a four-minute reporting period during each GMT hour, starting at 24 min 00 sec after the hour. Prior to deployment of the DCP to a field site, PL should request amendment of the July 1992 Memorandum of Agreement between NWRA and NESDIS. Any such request should be sent to the Data Collection and Direct Broadcase Branch of NOAA/NESDIS at the World Weather Building, Room 806, Washington, DC 20233.

5. CONCLUSION AND RECOMMENDATIONS

This SBIR contract has resulted in a prototype ITS now ready for delivery to Phillips Laboratory of Air Force Materiel Command. Consisting of its data-collection, data-retrieval, and central-processing subsystems, the prototype is ready for deployment and field testing (including beta testing of the central processor). The ITS10S receivers have been "field" tested by means of data recordings during passes of the NNSS satellites over NWRA's laboratory in Bellevue, WA. In addition, as a start on SBIR commercialization, two such receivers have been delivered to users. The data from Thule, Greenland, employed for testing Program 'prep_dat' were obtained from one of the two; the other has been delivered to a communications research laboratory in Japan.

From this work, we conclude that the WDLS procedure holds substantial promise for application to ionospheric tomography using relative TEC obtainable by means of existing satellites in low earth orbit. Aside from applying the technique to such data, we recommend that four productive steps be carried out now to advance the state of the art. First, the possibility should be explored that a background profile and corresponding EOFs tailored to specific observing conditions would further improve tomographic renderings. For the processor developed in this work, an efficient approach would be to incorporate functions from our existing model "database" for specific combinations of receiver-chain location, time of day, season, and sunspot number. Second, this approach then should be adapted to incorporate external field data such as a bottomside ionosonde profile. Third, a hybrid EOF/Fourier technique should be developed that would introduce into the problem the ionosphere's second natural coordinate system (with one axis aligned along the geomagnetic field).

Finally, it may be possible to increase the robustness of the WDLS technique substantially by addressing one of its most fundamental limitations as configured in our prototype ITS processor.

24

Aside from limitations inherent in satellite-to-surface geometry, we believe that its most basic limitation is its present inability to distinguish between over- and under-determined model parameters. The degree of under-determinacy damping introduced into our solutions determines the relative emphasis given to minimizing prediction error vs. minimizing solution length, but that damping is applied to model parameters without regard to their individual degree of determinacy. Linear-algebraic techniques exist for transforming model parameters and then partitioning them into over- and under-determined groups (Menke, 1989). If this could be achieved in the ionospheric case, we should be able to apply our a-priori information more judiciously to the under-determined group, solving for the over-determined parameters by minimizing prediction error in a uniquely least-squares sense. We suggest that developing such a partitioned WDLS processor could contribute substantially to the evolution of tomographic inversion into a robust tool for ionospheric research and monitoring.

References

Bent, R.B., S.K. Llewellyn, G. Nesterczuk, and P.E. Schmid, "The Development of a Highly Successful Worldwide Empirical Ionospheric Model and Its Use in Certain Aspects of Space Communications and World-wide Total Electron Content Investigations," *Effects of the Ionosphere on Space Systems and Communications*, ed. J. Goodman, National Technical Information Service, Springfield, VA, 1976.

Flattery, T.W. and A.C. Ramsay, "Derivation of Total Electron Content for Real-time Applications, *Effects of the Ionosphere on Space Systems and Communications*, ed. J. Goodman, National Technical Information Service, Springfield, VA, 1976.

Fremouw, E.J., "A Proposal to Develop a Prototype Ionospheric Tomography System," *NWRA-CR-90-P101*, Northwest Research Associates, Inc., Bellevue, WA, 1990.

Fremouw, E.J., "Conversion of ITS10 Receivers to ITS10S Capability for Recording Intensity and Dispersive-Phase Scintillation," *NWRA-CR-93-P209*, Northwest Research Associates, Inc., Bellevue, WA, 1993.

Fremouw, E.J., R.M. Bussey, "Central-Processor Computer Programs in the NWRA Prototype Ionospheric Tomography System (ITS)," *PL-TR-94-2265*, Geophysics Laboratory (Air Force Systems Command), Hanscom AFB, MA, 1994.

Fremouw, E.J. and J.M. Lansinger, "A Proposal to Develop an Ionospheric Tomography/Scintillation System (ITSS) for Remotely Sensing the Reconfiguration of Electron Density Due to Radio-Frequency (RF) Heating," *NWRA-CR-91-P109*, Northwest Research Associates, Bellevue, WA, 1991.

Fremouw, E.J. and J.M. Lansinger, "Development of a Prototype Ionospheric Tomography System," *R&D Status Report 2 on Project AFPL-0116*, Northwest Research Associates, Bellevue, WA, 1992a.

Fremouw, E.J. and J.M. Lansinger, "Development of a Prototype Ionospheric Tomography System," *R&D Status Report 5 on Project AFPL-0116*, Northwest Research Associates, Bellevue, WA, 1992b.

Fremouw, E.J., J.M. Lansinger, and J.A. Secan, "A Feasible Ionospheric Tomography System," *GL-TR-90-0353*, Geophysics Laboratory (Air Force Systems Command), Hanscom AFB, MA, 1990. ADB154713L

Hoots, F.R., and R.L. Roehrich, "Models for Propagation of NORAD Element Sets," *Spacetrack Report No. 3*, Defense Documentation Center, Alexandria, VA, 1980.

Jones, W.B., R.P. Graham, and M. Leftin, "Advances in Ionospheric Mapping by Numerical Methods," *ESSA Tech. Rep. ERL 107 - ITS 75*, U.S. Gov. Printing Office, Washington DC, 1969.

Lansinger, J.M., D.B. Keir, and E.J. Fremouw, "The NWRA ITS10S Coherent Radio Receiving System," *PL-TR-94-2264*, Geophysics Laboratory (Air Force Systems Command), Hanscom AFB, MA, 1994.

Menke, W, *Geophysical Data Analysis: Discrete Inverse Theory*, Academic, San Diego, CA, 1989.

Secan, J.A., "A Computer Model of the Electron Density Distribution in the Earth's Ionosphere," *NWRA-CR-90-R065/R1,* Northwest Research Associates, Inc., Bellevue, WA, 1980.

Secan, J.A., "Development of Techniques for the Use of DMSP SSIE Data in the AWS 4D Ionosphere Model," *PD-NW-85-327R*, Northwest Research Associates, Inc., Bellevue, WA, 1985.

Raymund, T.D., J.R. Austen, S.J. Franke, C.H. Liur, J.A. Klobuchar, and J. Stalker, "Application of Computerized Tomography to the Investigation of Ionospheric Structures," *Rad. Sci., 25*(5), pp. 771-790, 1990.

Rush, C.M., M. Fox, D. Bilitza, K. Davies, L. McNamara, F.G. Stewart, and M. Pokempner, "Ionospheric Mapping -- An Update for f_0F_2 Coefficients," *Telecomm. J. 56*, 1989.